

M2L TRANSLATION OPERATORS FOR KERNEL INDEPENDENT FAST MULTIPOLE METHODS ON MODERN ARCHITECTURES *

SRINATH KAILASA[†], TIMO BETCKE[‡], AND SARAH EL KAZDADI[§]

Abstract. Algorithm design must focus on minimising data movement even at the cost of more FLOPs due to the growing disparity between FLOP availability and memory bandwidth on modern architectures. We review the requirements for the Multipole to Local (M2L) operation, a sub-routine of the Kernel Independent Fast Multipole Method (kiFMM) algorithm. The kiFMM is a variant of the popular Fast Multipole Method (FMM), which accelerates the evaluation of N -body potential problems. Naively implemented, the M2L can lead to bandwidth pressure, and is therefore a key bottleneck in an FMMs. Recent software packages for the kiFMM have relied on the Fast Fourier Transform (FFT) to accelerate M2L as it can be formulated as a convolution type operation. However, parallelly developed ‘black box’ FMMs formulate the M2L as a BLAS operation and use direct matrix compression techniques for further acceleration. The FFT approach requires careful implementation to overcome the low operational intensity of the element-wise product inherent in its formulation, whereas the BLAS approach provides a high operational intensity formulation if the M2L is written in terms of level 3 BLAS operations. We describe algorithmic simplifications for the BLAS based M2L operation, and show that the BLAS version of the M2L can be competitive in practice with the Fast Fourier Transform (FFT) version. We have developed a carefully optimised software implementation that allows us to flexibly switch between M2L approaches and is optimised for ARM and x86 targets, allowing for a fair comparison between both.

Key words. FMM, High Performance Computing, M2L, Rust, multipole-to-local, kernel-independent FMM

MSC codes. 65-04, 65Y05, 65Y10, 65Y15, 65Y20

1. Introduction. The Fast Multipole Method (FMM) as originally presented by Greengard and Rokhlin [18] accelerates potential evaluation problems of the form

$$(1.1) \quad \phi_i = \sum_{j=1}^N K(\mathbf{x}_i, \mathbf{y}_j) q_j, \quad i = 1, \dots, M$$

where the potential ϕ_i is evaluated at a set of target points, $\{\mathbf{x}_i\}_{i=1}^M \in \mathbb{R}^d$, due to a set of densities, $\{q_i\}_{i=1}^N \in \mathbb{R}$, associated with a set of source points, $\{\mathbf{y}_j\}_{j=1}^N \in \mathbb{R}^d$. $K(\cdot, \cdot) : \mathbb{R}^d \times \mathbb{R}^d \rightarrow \mathbb{R}$ is the kernel specifying the nature of the interaction and d is the spatial dimension. In cases where the kernel is asymptotically smooth and non-oscillatory the FMM enables the evaluation of the sum (1.1) in $O(P(N + M))$ where $P \ll M, N$ is a parameter called the *expansion order* which controls the accuracy of the approximation. In comparison to a naive evaluation cost of $O(M \cdot N)$, the FMM enables a significant algorithmic speed-up.

N -body sums such as (1.1) appear across the computational sciences. For example, the evaluation of (1.1) with the Laplace kernel,

*Submitted to the editors February 20, 2025.

Funding: Srinath Kailasa is supported by EPSRC studentship 2417009, Timo Betcke is supported by EPSRC grants EP/W026260/1 and EP/W007460/1.

[†]Department of Mathematics, University College London, London, UK. (srinath.kailasa.18@ucl.ac.uk).

[‡]Department of Mathematics, University College London, London, UK (t.betcke@ucl.ac.uk)

[§](sarahelkazdadi@gmail.com)

$$(1.2) \quad K(\mathbf{x}, \mathbf{y}) = \begin{cases} \frac{1}{2\pi} \log\left(\frac{1}{\|\mathbf{x}-\mathbf{y}\|}\right), & (d = 2) \\ \frac{1}{4\pi\|\mathbf{x}-\mathbf{y}\|}, & (d = 3) \end{cases}$$

corresponds to the evaluation of electrostatic or gravitational potentials where the source densities are static charges, or masses. However, similar sums also appear in the evaluation of dense operator matrices in the boundary integral formulation of partial differential equations with applications from geoscience [16] and fluid simulation [27], to data analysis and machine learning [21, 3].

The FMM achieves its acceleration through a recursive partition of the problem domain and finding an appropriate compressed representation of the *far field* corresponding to distant *clusters* of source points evaluated at a cluster of target points. In this way the number of computations which rely on expensive direct evaluations of (1.1) is reduced to the *near field* of each cluster of target points. This trade-off between far and near field computation characterises the performance of the FMM. With as a rule of thumb far-field interactions resulting in bandwidth pressure, and near field interactions resulting in compute pressure.

Since its original formulation hardware has evolved significantly. Modern architectures even more strongly favour algorithms which incorporate a high rate of data re-use per FLOP and data parallel implementations in order to take advantage of multiple compute cores [14]. As a result, sums of the form (1.1) can be performed highly efficiently as the sum is trivially parallel over target points. Indeed, in Table 1.1 we see that on commodity CPUs we can now compute the interaction of one hundred thousand points in under a second in single precision if carefully optimised for SIMD and memory caching. This level of performance for the direct evaluation of (1.1) has consequences for the optimal implementation of FMMs as we are now principally limited by the bandwidth intensive handling of far field interactions for each cluster of target points. This algorithmic subroutine is called the Multipole to Local (M2L) operation the optimisation of which is the focus of this paper in the context of the Kernel Independent Fast Multipole Methods (kiFMMs), a popular variant of the FMM algorithm.

The kiFMM has been preferred in recently presented high-performance software implementations due to its straightforward formulation [23, 31] that relies on simple linear algebra operations as opposed to complex analytical field translations in earlier FMM implementations. However, the linchpin is the efficient evaluation of the M2L operation, for which the best available implementations of the kiFMM rely on Fast Fourier Transform (FFT) acceleration due to the convolution type of the M2L in the kiFMM. We call this approach the FFT-M2L in the remainder of this paper, its algorithmic and implementation details are summarised in Appendix A. The FFT-M2L approach achieves high performance. But convolution type operations result in a bandwidth limited element-wise products. Handling this requires careful memory layout optimisations with explicit SIMD programming to achieve practical performance.

Parallel progress in so-called Black Box Fast Multipole Methods (bbFMMs) based on Chebyshev interpolation of kernels [15, 24] represent the M2L operation as direct matrix operation and use low-rank compression techniques to accelerate its evaluation. In the following we simply call this variant of M2L translation BLAS-M2L. The advantage of the BLAS-M2L is that it is algorithmically easier than the FFT-M2L and requires less involved memory reorderings to become efficient. BLAS operations

are increasingly optimised at software level [29], with co-design reflected at hardware level [10, 17]. It is increasingly favourable to formulate classical algorithms as BLAS operations to exploit these developments. However the BLAS-M2L approach depends strongly on the low-rank compressibility of the matrices that arise for the M2L operation, which makes this approach far more efficient for the FMM in two dimensions than in three dimensions.

We investigate whether the BLAS-M2L can be competitive with respect to the FFT-M2L for the kiFMM in three dimensions for the Laplace kernel (1.2) on modern CPUs. In order to provide a fair environment for comparison we have developed our own kiFMM implementation using Rust as a modern performant low-level language¹. Our implementation based on Rust’s ‘trait’ system enables the selection of different implementations of the M2L operation at type level without dynamic runtime overhead. We have made sure to carefully optimise the implementation to achieve similar levels of performance as PVFMM [23] in order to have a good baseline for benchmarking.

We demonstrate that our BLAS-M2L approach is not only competitive with the highly optimised FFT-M2L approach of recent software, but in fact preferable for high accuracy evaluations in double precision. This is largely due to the high *operational intensity* [32] of the BLAS-M2L method² which increases as a function of matrix size as opposed to the more bandwidth limited FFT-M2L implementation.

Our main contributions can be summarised as follows.

- A description of algorithmic improvements to speed-up BLAS based M2L operators, improve cache re-use and maximise operational intensity.
- Extensive numerical benchmarking of the FFT-M2L against the BLAS-M2L using our own kiFMM implementation for the Laplace kernel in three dimensions.

We begin in Section 2 by reviewing the basics of the kiFMM. In Section 3 we describe the implementation of BLAS-M2L, discussing data layout, compression techniques and tricks to speed up the setup and runtime computations. In Section 4 we provide a summarised comparison of the BLAS-M2L and FFT-M2L approaches. In Section 5 we provide single node benchmarks, followed by a reflection on our results in Section 6.

1.1. Related Work. Relatively few past works have focussed on optimisations of the M2L operation for non-oscillatory kernel functions for the kiFMM, where it appears as a series of dense matrix vector products, which by choice of discretisation can optionally be accelerated with an FFT. In the original presentation [33], a BLAS-M2L approach is dismissed for problems in three spatial dimensions citing insufficient decay in rank of the matrices associated with the M2L operation, and the costs associated with low rank compression based on the SVD. They instead propose the FFT-M2L in this situation, which was optimised for x86 CPUs by PVFMM [23] and re-implemented in later works such as the latest version of ExaFMM [31]. We describe the FFT-M2L approach in Appendix A, where we also derive estimates for its operational intensity. We note that in order for this approach to obtain high

¹Our software can be found at <https://github.com/bempp/kifmm/>

²We define operational intensity as the number of operations performed per unit of data retrieved from *main memory* and subsequently filtered through a processor’s cache hierarchy [32]. Thus operational intensity is characterised by the traffic between a processor’s cache and main memory, rather than *within* the cache hierarchy of a processor - which is usually captured by a related concept called *arithmetic intensity*. We prefer operational intensity in comparison to arithmetic intensity as the data we are concerned with is often too large to fit into a processor’s cache.

Precision	Number of Points	Apple M1 Pro	AMD 3790X
Single Threaded			
Single	5,000	11 (ms)	11 (ms)
	20,000	180 (ms)	171 (ms)
Double	5,000	28.2 (ms)	25 (ms)
	20,000	45.00 (ms)	401 (ms)
Multi Threaded			
Single	20,000	30 (ms)	6 (ms)
	100,000	820 (ms)	148 (ms)
	500,000	21.80 (s)	4 (s)
Double	20,000	79 (ms)	13 (ms)
	100,000	2.2 (s)	308 (ms)
	500,000	56.1 (s)	11 (s)

Table 1.1: Runtimes for single and multi threaded direct $O(N^2)$ evaluation of the Laplace kernel in the optimised implementation provided by our Green Kernels library [6] for the CPUs listed in Table C.2. We consider the source and target points to be the same set. Our implementation of the Laplace kernel closely follows that first presented in [23], using explicit SIMD programming and Newton iterations for the calculation of fast square roots in the kernel function [6]. In multithreaded experiments we pin one logical thread to each physical core available on the architectures tested.

runtime performance tailored implementations are required for each Instruction Set Architecture (ISA).

Our work is principally based on that presented for the bbFMM [15] which introduced methods to reduce the cost of low-rank compression of matrices associated with the M2L operation based on the SVD for non-oscillatory kernel functions. This is extended in the work of Messner et al, who optimise the compression schemes for non-oscillatory kernels based on the SVD to address the high associated setup costs [24], as well as blocking strategies for CPU based implementations to ensure high operational intensity in the matrix-matrix products for the M2L operation. These strategies form the core of their ScalFMM and TBFMM implementations in their group [9, 7, 2]. Takahashi et al also developed an early GPU implementation of the M2L operation for the kiFMM based on similar techniques involving blocking multiple M2L operations together [28]. They obtain good results especially in single precision, however the blocking schemes presented are complex and limited by the small GPU memories and associated data organisation costs of their time as well as the lack of contemporary batched-BLAS implementations for GPUs such as [26].

The approach to data organisation for the BLAS-M2L presented in this paper is significantly simpler in structure in comparison to previous approaches, reducing the number of BLAS calls to a minimum and making a heterogeneous adaption based on batched-BLAS straightforward. Furthermore, our software framework allows us to perform a direct comparison with FFT-M2L for the kiFMM. To the best of our knowledge there has been no direct comparison, though similar work has been conducted for the analytical FMM based on multipole expansions [12, 13].

2. Fast Multipole Method. FMMs rely on degenerate approximations of the kernel $K(\cdot, \cdot)$, such that the potential (1.1) when evaluated between distant clusters

of target and source points can be expressed as a sum

$$(2.1) \quad \phi_i \approx \sum_{p=1}^P \sum_{j=1}^N A_p(\mathbf{x}_i) B_p(\mathbf{y}_j) q_j, \quad i = 1, 2, \dots, M,$$

where the expansion order P is chosen such that $P \ll M, N$. The functions A_p and B_p are determined by the approximation scheme used by an FMM method. In the original presentation the evaluation of,

$$\hat{q}_{j,p} = \sum_{j=1}^N B_p(\mathbf{y}_j) q_j, \quad p = 1, 2, \dots, P$$

corresponded to the construction of an analytical expansion of the kernel function which represented the potential due to the set of source points [18]. The calculation,

$$\phi_i \approx \sum_{p=1}^P A_p(\mathbf{x}_i) \hat{q}_{p,j}, \quad i = 1, 2, \dots, M$$

represented the evaluation of this potential at the set of target points.

The accuracy of the approximation (2.1) depends on a sufficient distance between clusters of sources and targets, referred to as *admissibility*. FMMs therefore split (1.1) for a given target cluster into *near* and *far* components

$$(2.2) \quad \phi_i = \sum_{\mathbf{y}_j \in \text{Near}(\mathbf{x}_i)} K(\mathbf{x}_i, \mathbf{y}_j) q_j + \sum_{\mathbf{y}_j \in \text{Far}(\mathbf{x}_i)} K(\mathbf{x}_i, \mathbf{y}_j) q_j$$

the latter of which are taken to be admissible and can be approximated by (2.1) with the near component evaluated directly.

Linear asymptotic complexity is achieved by partitioning the problem domain with a hierarchical data structure, commonly an octree in three dimensions or a quadtree in two dimensions, where a bounding box is placed over all sources and targets and recursively subdivided into equal sub-boxes, called its children. For a box σ with side length d centred at c , we define its near field \mathcal{N}_σ as all boxes that lie within a box of side length $3d$ centered at c , including σ itself. Its far field \mathcal{F}_σ is the complement of this. The idea is then to compress evaluation of interactions for each target box where a source box can be considered admissible, ie. in its far field, by using approximations to represent the field generated by far-field boxes. The approximations for potential due to a set of source densities are encoded using *multipole* and *local* expansions. Multipole expansions are used to describe potentials in the exterior of given box generated from sources in that box, and local expansions are used to describe potentials inside a box generated by sources in its far-field. The terms ‘multipole’ and ‘local’ are common terminology across methods derived from the FMM, even those which use an alternative approximation scheme. For octrees we refer to adjacent boxes, which share a face, edge, or vertex as *neighbours*, the eight child boxes of a given box, σ , as *siblings*. Translations between these expansion representations are what gives the FMM its complexity, in particular,

- **multipole to multipole (M2M)**: Translation of the multipole expansion of a child box to one centered on its parent box. This allows the accumulation of a multipole expansions representing child boxes as one traverses the tree from finest to coarsest level.
- **multipole to local (M2L)**: Translation of the multipole expansion of a source box into a local expansion of a non adjacent target box whose parent is a neighbour of the source box’s parent. Such boxes for a given box, σ , are admissible and are referred to as its *interaction list*, I_σ . In three dimensions $|I_\sigma| \leq 189$.
- **local to local (L2L)**: Translation of a local expansion of a parent box, to one centered on a child box. This allows the accumulation of a local expansion representing ancestor boxes as one traverses the tree from coarsest to finest level.

The algorithm for non-oscillatory kernels, based on *uniform refinement* such that all leaf boxes are of the same size, proceeds in a recursive two step procedure.

1. **Upward Pass**: First multipole expansions are encoded for boxes at the leaf level, in a Particle to Multipole (P2M) step. We then recurse by level, from finest to coarsest boxes, applying the M2M translation to each one.
2. **Downward Pass**: The tree is then traversed from coarsest to finest boxes, the local expansion is accumulated from both (i) a box’s parent (L2L) and (ii) source boxes in its interaction list (M2L). Specified in this way, the local expansion encodes the potential at a box σ due to boxes in \mathcal{F}_σ . At the leaf level, the local expansion is evaluated at target points in each leaf box (L2P) and the potential due to adjacent boxes is calculated directly using (1.1) known as the Particle to Particle (P2P) operation.

We see that during the upward and downward passes, each target box interacts with a fixed number of source boxes. Indeed, an octree for a set of points N discretised such that each of leaf box contains a bounded number of points, results in $\sim N$ leaf boxes and depth $\log_8(N)$ contains $O(N)$ boxes in total, giving a runtime complexity of $O(\kappa N)$, where κ is a scalar constant that depends on the number of interactions for the M2L and P2P operations.

2.1. Performance Characteristics of the FMM. FMM performance is determined by the implementations of the M2L and P2P operations during the downward pass. The P2P operation is compute bound and is naturally expressed using either SIMD or SIMT paradigms as the evaluations per target are independent of each other. Choosing relatively smaller degrees of refinement for the hierarchical data structure results in a large near field calculations for each leaf box, which can be performed quickly for moderate problems sizes as we show in Table 1.1.

The M2L when implemented naively results in non-contiguous memory access patterns and resulting cache misses from having to index data corresponding to potentially discontinuous boxes in the hierarchical tree [11]. The fact that each box needs to perform up to 189 M2L translations in three dimensions leads the M2L operation to dominate runtime for deep trees. This trade-off between shallow trees and P2P bound implementations and deep trees with M2L bound implementations characterises the performance of the FMM.

We note that the performance of our P2P implementation alleviates the need for *adaptive refinement* of the hierarchical data structure, in which leaf boxes are refined until they contain fewer than a user-specified threshold of points. Previously adaptive FMMs have been recommended for highly non-uniform point distributions, and are

used to limit the P2P operation by increasing the number of admissible source boxes which may ostensibly be in the near field of a target box as defined above but are refined to a greater extent and therefore amenable to compression. However, this approach requires additional interaction lists which must be calculated at runtime from the point data [33] as well as deeper trees to cope with the extreme point distributions. Ensuring contiguous data access is the most significant challenging when handling interaction lists and deeper trees make FMMs bound by the performance of the M2L implementation. In our implementation we instead use a weaker form of adaptivity, whereby branches which contain no point data are pruned.

2.2. Kernel Independent Fast Multipole Method.

2.2.1. Forming Multipole and Local Expansions. We review the kiFMM of Ying. et. al [33], which makes use of the Method of Fundamental Solutions (MFS) for field approximations. Consider the construction of a ‘multipole’ expansion corresponding to a set of source densities in a box σ , as in the left plot of Figure 2.1. We begin by constructing an ‘equivalent surface’ discretised by a set of evenly spaced points \mathbf{y}_j with associated ‘equivalent densities’, q_j . We match the field generated by these to that generated by the true source densities at a further enclosing ‘check surface’ represented by discrete points \mathbf{x}_i to arrive at the equation

$$(2.3) \quad \sum_j K(\mathbf{x}_i, \mathbf{y}_j) q_j = \phi^{\sigma, u}(\mathbf{x}_i)$$

where $\phi^{\sigma, u}$ is the (upward) ‘check potential’ generated by the sources in σ . This gives the matrix equation

$$(2.4) \quad \mathbf{K}\mathbf{q} = \boldsymbol{\phi}$$

where \mathbf{K} is an $N_{\text{check}} \times N_{\text{equiv}}$ matrix with entries $K(\mathbf{x}_i, \mathbf{y}_j)$ with $\mathbf{x}_1, \dots, \mathbf{x}_{N_{\text{check}}}$ the evaluation points on the check surface and $\mathbf{y}_1, \dots, \mathbf{y}_{N_{\text{equiv}}}$ the source points on the equivalent surface. N_{check} and N_{equiv} are the number of evaluation points on the check surface and source points on the equivalent surface respectively. Equation (2.4) defines an ill-conditioned least-squares problem, which we solve using the ‘backward-stable’ pseudo inverse first presented in [23] to find the equivalent densities \mathbf{q} ³.

$$(2.5) \quad \begin{aligned} \mathbf{q} &= (\mathbf{K})^\dagger \boldsymbol{\phi} \\ &= \mathbf{V}_\varepsilon (\boldsymbol{\Sigma})_\varepsilon^{-1} \mathbf{U}_\varepsilon^T \boldsymbol{\phi} \\ &= \mathbf{V}_\varepsilon \tilde{\mathbf{U}}_\varepsilon^T \boldsymbol{\phi} \end{aligned}$$

Greater accuracy is maintained by storing separately the components of the pseudo inverse, where ε is a threshold for singular values beyond which associated

³In [23] it is noted that there are two sources of error in computing equivalent densities. The first is a round-off error in the check potential, which is amplified by a factor equal to the condition number of the inverted matrix. The second is from multiplying the factors of the pseudo inverse itself together, due to the large range in the singular values. The first error is damped by a similar factor when computing a far field potential using an equivalent density, and therefore does not significantly effect the final computed potential using the kiFMM. However, the second error source can be mitigated by storing the pseudo inverse in two components where the diagonal matrix of singular values is multiplied with one of the two orthonormal matrices of left or right singular vectors

singular vectors are filtered out. Our pseudo inverse implementation closely mirrors that of SciPy [30]. Considering a matrix of size $M \times N$ for which we are computing our pseudo inverse defining $d = \max(M, N)$, α (absolute tolerance) as a user specified value, ρ (relative tolerance) as $\rho = d \cdot \varepsilon_{\text{mach}}$ where $\varepsilon_{\text{mach}}$ is machine precision and letting σ_0 represent the largest singular value, the threshold ε is computed as,

$$(2.6) \quad \varepsilon = (\alpha + \rho) \cdot \sigma_0.$$

We find heuristically good performance by setting $\alpha = 0$.

One can construct local expansions using the surfaces defined in the right plot of Figure 2.1, where now the check surface must be enclosed by the equivalent surface.

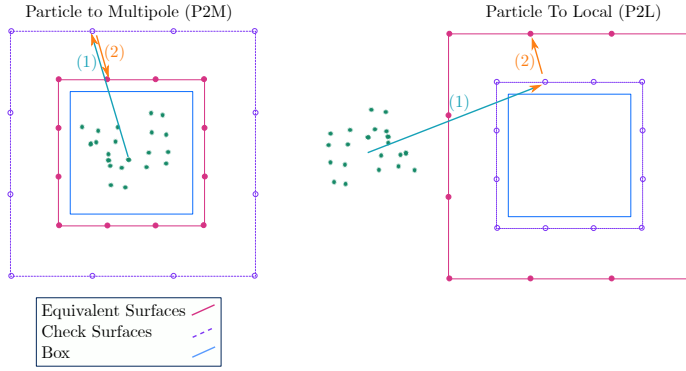


Fig. 2.1: We illustrate the surfaces, and their associated discretisation points, required to construct multipole and local expansions from source points, shown in green. This is for a problem in \mathbb{R}^3 , where we have taken $P = 4$. We show cross sections of cubic surfaces, as in Figure 4 of [33], where source points are shown as green points. The arrows illustrate the steps of the calculation (1) compute the check potential from the source points (2) calculate the equivalent densities using the check potentials.

2.3. Translation Operators. The M2M, L2L and M2L operators are formed using the same technique as above, and are illustrated in Figure 2.2. For the M2M and L2L, forming the required surfaces, we match the field generated by the child/parent box's equivalent densities at the parent/child box's check surface respectively to find the check potential. This results in equations of the form of (2.5) for the calculation of the the multipole/local expansions, respectively.

We explicitly show the procedure for the M2L operator. Denote by \mathbf{x}_i the points discretising the downward check surface of the target box τ . We first need to evaluate the field generated at \mathbf{x}_i through the equivalent surface of the source box σ . This can be written as the matrix product

$$\boldsymbol{\phi}^{\sigma, \tau} = \mathbf{K}_{\sigma, \tau} \mathbf{q}^{\sigma}$$

with $[\mathbf{K}_{\sigma, \tau}]_{i, j} = K(\mathbf{x}_i, \mathbf{y}_j)$ and the vector \mathbf{q}^{σ} containing the associated equivalent source densities in σ . Let us now introduce the matrix \mathbf{K}_{τ} , which contains the kernel interaction between the discretisation points on the equivalent surface and the check surface for τ . The equivalent density \mathbf{q}^{τ} is now obtained through

$$(2.7) \quad \mathbf{q}^{\tau} = (\mathbf{K}_{\tau})^{\dagger} \sum_{\sigma \in I_{\tau}} \mathbf{K}_{\sigma, \tau} \mathbf{q}^{\sigma},$$

where the sum is over all source boxes σ in the interaction list I_τ of τ .

The calculation (2.7) corresponds to a series of dense matrix-vector products, where the matrix $\mathbf{K}_{\sigma,\tau}$ is known to be of low rank due to the properties of the kernel function used to construct it. It is therefore amenable to numerical compression techniques such as the SVD. Alternatively, for kernels which are translation invariant such that $K(\mathbf{x}, \mathbf{y}) = K(\mathbf{x} - \mathbf{y})$, by choosing the upward equivalent and downward check surfaces to be defined equivalently with respect to a given box, the evaluation of the check potential can be interpreted as a three dimensional convolution and can therefore be accelerated with a Fast Fourier Transform (FFT). We note that $(\mathbf{K}_\tau)^\dagger$ depends only on the downward equivalent and check surfaces of a box, if these are chosen to be the same relative to a given box, this matrix can be cached, and depending on kernel properties, scaled at each level of the tree.

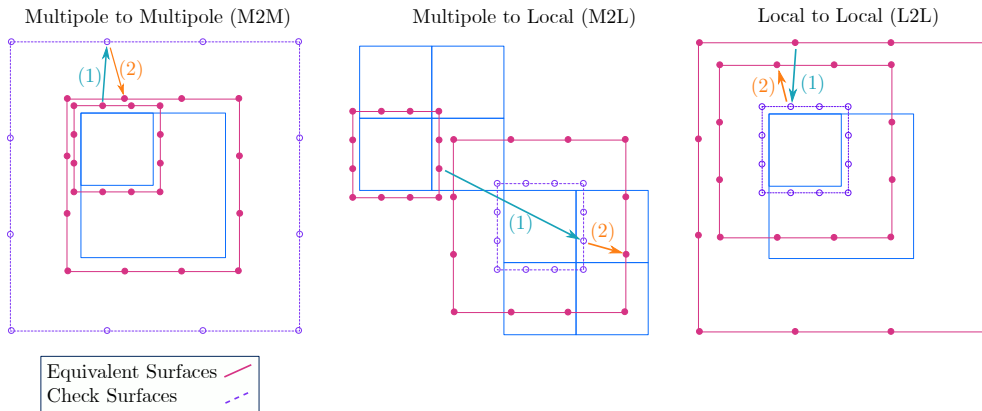


Fig. 2.2: We illustrate the surfaces, and their associated discretisation points, required to perform each field translation, M2M, M2L and L2L. This is for a problem in \mathbb{R}^3 , where we have taken $P = 4$. We show cross sections of cubic surfaces, as in Figure 5 of [33]. We show how for the M2L, the source box’s equivalent surface and the target box’s check surface can be seen to originate from a regular Cartesian grid, enabling the acceleration in the computation of the check potential in this case via the FFT. The arrows illustrate the flow of the calculation (1) compute the check potential (2) evaluate the equivalent density using the check potential.

3. BLAS based M2L Operators for the Laplace Kernel.

3.1. Algorithm Setup. In order to accelerate the evaluation of (2.7) we seek to compress the associated matrices $\mathbf{K}_{\sigma,\tau}$ with each M2L translation numerically, which we call the M2L matrices in the following. We build upon the ideas first presented in [15, 24] for the Black Box Fast Multipole Method (bbFMM), based on an alternative Chebyshev based approximation scheme. Each source/target box pair corresponds to a relative orientation between the boxes which we describe with a transfer vector $t \in T_l$ where T_l is the set of all unique transfer vector at a level $l \in [0, d]$ of an octree of depth d .

We note that the size of the set $|T_l| \leq 316$ at a given level l of an octree for the Laplace kernel. This can be seen by considering the interactions of a given target box, τ , and its siblings together. Each sibling box’s near field consists of $27 = 3^3$ boxes including itself, with which it shares an edge, a face or a vertex. From the definition of

admissible boxes, a given target box's far field consists of $189 = 6^3 - 3^3$ boxes, where 6^3 comes from the fact that the interaction list of each box must lie within the near field of τ 's parent, which has a width of 6 boxes in units of its child boxes. Similarly, the union of all possible relative positions corresponding to interactions between each sibling and child boxes in the near field of its parent can be seen to be 7^3 . Accounting for the relative positions for near field interactions which are common to each sibling, we see that there are at most $316 = 7^3 - 3^3$ unique relative positions for translationally invariant kernels for which $K(\mathbf{x} - \mathbf{y}) = K(\mathbf{x}, \mathbf{y})$, such as the Laplace kernel.

We identify each M2L matrix with a transfer vector \mathbf{K}_t , and assemble a $N_{\text{check}} \times |T_l| \cdot N_{\text{equiv}}$ matrix row-wise,

$$\mathbf{K}_{\text{fat}} = [\mathbf{K}_1 \quad \dots \quad \mathbf{K}_{|T_l|}]$$

and a $|T_l| \cdot N_{\text{check}} \times N_{\text{equiv}}$ matrix column-wise

$$\mathbf{K}_{\text{thin}} = \begin{bmatrix} \mathbf{K}_1 \\ \dots \\ \mathbf{K}_{|T_l|} \end{bmatrix}.$$

These are then compressed using SVDs, providing a rank- k approximation,

$$(3.1) \quad \mathbf{K}_{\text{fat}} \approx \mathbf{U} \boldsymbol{\Sigma} \begin{bmatrix} \mathbf{V}_1^T & \dots & \mathbf{V}_{|T_l|}^T \end{bmatrix} = \mathbf{U} \boldsymbol{\Sigma} \tilde{\mathbf{V}}^T,$$

$$(3.2) \quad \mathbf{K}_{\text{thin}} \approx \begin{bmatrix} \mathbf{R}_1 \\ \dots \\ \mathbf{R}_{|T_l|} \end{bmatrix} \boldsymbol{\Lambda} \mathbf{S}^T = \tilde{\mathbf{R}} \boldsymbol{\Lambda} \mathbf{S}^T.$$

\mathbf{U} is of size $N_{\text{check}} \times k$ and \mathbf{S} is of size $N_{\text{equiv}} \times k$ and k is chosen such that we achieve a desired accuracy of ε in the final evaluated potential.

From [15], considering each element of \mathbf{K}_{fat} and \mathbf{K}_{thin} corresponding to a given $t \in T_l$, and using that \mathbf{S} and \mathbf{U} have orthonormal columns, we obtain

$$(3.3) \quad \mathbf{K}_t = \mathbf{U} \mathbf{C}_t \mathbf{S}^T,$$

where

$$\mathbf{C}_t = \mathbf{U}^T \mathbf{K}_t \mathbf{S}$$

is of size $k \times k$ and is called the *compressed M2L matrix*, which operates on the *compressed multipole expansion*,

$$\tilde{\mathbf{q}} = \mathbf{S}^T \mathbf{q}$$

and returns the *compressed check potential*

$$\tilde{\mathbf{q}} = \mathbf{C}_t \mathbf{S}^T \mathbf{q} = \mathbf{C}_t \tilde{\mathbf{q}}.$$

Examining the singular values of \mathbf{K}_{fat} and \mathbf{K}_{thin} of dimension $M \times N$ for the three dimensional Laplace kernel one observes that approximately $k \sim \max(M, N)/2$ is sufficient for obtaining machine precision relative errors in both single and double precision in the final evaluated potential as shown in [15]. We find that in practice we can often obtain significantly greater compression than this when solving for a lower level of accuracy as we discuss in Section 5. For kernels which are symmetric such that $\mathbf{K}_{\text{fat}} = \mathbf{K}_{\text{thin}}^T$ where the check and equivalent surfaces are discretised to the same degree we can compute just a single SVD. If a kernel is *homogenous* such that

$K(\alpha\mathbf{x}, \alpha\mathbf{y}) = \alpha K(\mathbf{x}, \mathbf{y})$ such as the Laplace kernel we see that we need only compute the SVD *once*, with the resulting M2L matrices re-used and scaled at each level.

Messner and co-workers notice that as the value of k is dictated by the highest rank interaction in T_l the cost of the applying \mathbf{C}_t can be further reduced with another SVD for each individual \mathbf{K}_t for $t \in T_l$ [24],

$$(3.4) \quad \mathbf{C}_t \approx \bar{\mathbf{U}}_t \bar{\boldsymbol{\Sigma}}_t \bar{\mathbf{V}}_t^T = \bar{\mathbf{U}}_t \bar{\mathbf{V}}_t'^T$$

where $\bar{\mathbf{U}}_t$ and $\bar{\mathbf{V}}_t'$ are of size $k \times k_t$ and $\bar{\boldsymbol{\Sigma}}$ is of size $k_t \times k_t$ and k_t again chosen to preserve a given relative error ε in the evaluated potential. In order to determine k and k_t we perform a grid search to determine the optimum parameters to achieve a given relative error ε in the evaluated potentials, the results of which are described in Table C.3 in Appendix C.

In our BLAS-M2L approach we identify *all* matching source/target box pairs in each level of an octree $l \in [2, d]$ during the downward pass by their transfer vector, grouping together the computation of their check potentials as a *single matrix-matrix product* for each transfer vector at each level l . The large size of these matrix-matrix products is naturally of high operational intensity.

This is in contrast to previous BLAS-M2L schemes such as that described in [24], where the symmetry and translational invariance properties of the kernel are used to permute the M2L matrices for a given source/target box pair to form matrix-matrix products. Further blocking was accomplished by blocking over sets of sibling boxes.

With this we can compute all check potentials for target boxes in a given level in at most $2 \times |T_l| = 634$ level 3 BLAS calls for translationally invariant kernels. High performance is enabled by the powerful optimisations implemented by modern BLAS variants [29, 1, 26], automatically configuring tiling schemes for the memory hierarchy of a particular device and applying optimisations such as loop re-ordering and SIMD vectorisation.

Computing the SVDs required by our scheme is costly in comparison to the setup of the FFT-M2L, especially for high expansion orders in double precision. We address this by using the Randomised Singular Value Decomposition (rSVD) [19], in contrast the deterministic SVDs used in the past [24]. We only consider ‘one shot’ rSVDs that avoid slow power iterations which repeatedly apply QR decompositions to compute the orthonormal basis of the subspace into the subspace into which the matrix to be compressed is being projected, instead only relying on oversampling and our knowledge of the low-rank nature of our kernel to improve the performance of the rSVD. Specifically, we use the result that \mathbf{K}_{fat} and \mathbf{K}_{thin} if of dimension $M \times N$ are approximately of rank $k \sim \max(M, N)/2$ for the Laplace kernel as found in [15], computing the rSVD with this rank estimate. We provide an overview of the rSVD parameters used in Table C.3 Appendix C for achieving a given relative error ε in the evaluated potential.

We note that the SVDs required during the directional compression step (3.4) are relatively cheap in comparison to that for \mathbf{K}_{fat} and \mathbf{K}_{thin} and therefore use only the classical SVD here while retaining reasonable setup times, which we document in Table C.3.

3.2. Algorithm. We can summarise our approach for the M2L operation for each target box τ at each level $l \in [2, d]$ during the downward pass as follows.

1. For each transfer vector (associated with index t) collect all corresponding source/target box pairs as a map. This is part of the precomputation. Let

N_t be the number of source boxes associated with t . By N_σ we denote the number of all source boxes in the tree on level ℓ .

2. For all N_σ source boxes compute the compressed multipole expansions. This is done through a single BLAS3 call of the form

$$[\tilde{\mathbf{q}}_1, \dots, \tilde{\mathbf{q}}_{N_t}] = \mathbf{S}^T[\mathbf{q}_1, \dots, \mathbf{q}_{N_t}]$$

3. Allocate up to 316 buffers to store each of the N_t compressed multipole expansions associated with each transfer vector $t \in [1, 316]$ contiguously, noting that not all transfer vectors may appear in interaction lists at a given level. Each buffer is of the form,

$$[\tilde{\mathbf{q}}_1, \dots, \tilde{\mathbf{q}}_{N_t}]$$

This requires using the results of Step 1, where we identify transfer vectors associated with each source box, which can be used to lookup their associated data.

4. Compute the compressed check potentials in a loop over each $t \in [1, 316]$, resulting in up to 632 level 3 BLAS calls, as not all transfer vectors may appear in interaction lists at a given level,

$$\begin{aligned} [\boldsymbol{\xi}_1, \dots, \boldsymbol{\xi}_{N_t}] &= \bar{\mathbf{V}}_t'^T[\tilde{\mathbf{q}}_1, \dots, \tilde{\mathbf{q}}_{N_t}] \\ [\tilde{\boldsymbol{\phi}}_1, \dots, \tilde{\boldsymbol{\phi}}_{N_t}] &= \bar{\mathbf{U}}_t[\boldsymbol{\xi}_1, \dots, \boldsymbol{\xi}_{N_t}], \end{aligned}$$

where we have used the re-compressed form of \mathbf{C}_t calculated with (3.4). We note that in implementations these two multiplications can be performed in place and that the product $\bar{\mathbf{V}}_t'^T = \bar{\boldsymbol{\Sigma}}_t \bar{\mathbf{V}}_t^T$ should be pre-calculated.

5. Each $\tilde{\boldsymbol{\phi}}_i$ is associated with a source box at level ℓ i.e. contained in an interaction list of any target box at this level. These are accumulated in a buffer containing N_τ compressed check potentials associated with the N_τ target boxes at level ℓ . We now compute with another BLAS call the corresponding uncompressed check potentials.

$$[\boldsymbol{\phi}_1, \dots, \boldsymbol{\phi}_{N_\tau}] = \mathbf{U}[\tilde{\boldsymbol{\phi}}_1, \dots, \tilde{\boldsymbol{\phi}}_{N_\tau}].$$

Once the check potentials are found, we can recover the local expansions at each target box using a calculation of the form of (2.7).

The entire scheme for computing the check potentials at each tree level ℓ during the downward pass, consists of up to 634 matrix-matrix multiplications per level, including the conversion into the compressed multipole expansion, the calculation of the compressed check potentials, and the conversion of the compressed check potential back into the check potential. If we choose to avoid the re-compression of \mathbf{C}_t during Step 4 the scheme uses 318 matrix-matrix multiplications per level.

The organisation of matrix-matrix multiplications in Step 4 is up to the choice of an implementer. In a CPU implementation, if a particular architecture contains a large number of CPU cores we find good performance by partitioning the multiplications for each $t \in [1, 316]$ over threads and performing them each in single threaded mode. In this case instruction level and data prefetching optimisations of the BLAS library are still enabled. Conversely if a CPU architecture has limited numbers of cores such as on standard desktops and laptops we find good performance with the

multiplications themselves performed multithreaded while we loop serially over each transfer vector.

The only runtime data organisation required is the allocation of buffers in Step 3, and the accumulation of data for each target box in Step 5. Both of these steps can be parallelised with multithreading, as data for each source and target box are not overlapping in memory. The scheme is also readily adapted into a GPU based implementation, especially if a particular architecture supports coherent memory access between the CPU and GPU. The data organisation can be made to take place on the CPU with the matrix-matrix multiplications deferred to the GPU which support batch BLAS [26], with minimal data transfer costs.

We defer to the underlying BLAS implementation to apply instruction level optimisations, and maximise operational intensity. Instead, we simply ensure that the data accesses required by the BLAS calls are contiguous. Importantly, this approach allows us to easily compute the FMM for *multiple sets of source densities* sharing a set of target and source points, common in the application of FMMs to boundary integral equations. We simply identify all common translations corresponding to each right hand side of (1.1) at a given level, and pass them through the level 3 BLAS operations, letting the underlying BLAS library handle the required blocking for this larger calculation. We provide an algorithmic analysis of the runtime in Appendix B to find estimates for the operational intensity of our method. The key point to note is that the operational intensity of the convolution step of our BLAS-M2L method in Step 4 in which we calculate the compressed check potentials in the above algorithm from (B.4) is given as,

$$\frac{2 \cdot 8^l \cdot k \cdot k_t}{8^l \cdot k + k_t \cdot k + 2 \cdot 8^l \cdot k_t} + \frac{2 \cdot 8^l \cdot k \cdot k_t}{8^l \cdot k_t + k_t \cdot k + 2 \cdot 8^l \cdot k} \text{ FLOPs/Accesses.}$$

Assume for simplicity that $k = k_t$. Then the above expression results in

$$\frac{4 \cdot 8^\ell k}{3 \cdot 8^\ell + k},$$

which shows that the FLOPs/Accesses increases with growing k , which is especially advantageous for the higher ranks in three dimensional FMMs.

4. Comparison With the FFT-M2L. From the central plot of Figure 2.2 we can consider the evaluation of the check potential at a target box as a convolution of the equivalent densities at each source box in its interaction list with the M2L matrix evaluated between the source box’s equivalent surface and the target box’s check surface if the surfaces are discretised to the same degree. This convolution is accelerated with the FFT, however this relies on an element-wise Hadamard product, which is of low operational intensity as the number of memory accesses is proportional to the number of FLOPs in this operation.

The major contribution of the PVFMM software was a formulation of the Hadamard product to achieve high computational throughput despite the low operational intensity. The method is described in detail in Appendix A, which shows how the expected *arithmetic intensity*, defined as the ratio of FLOPs to memory accesses from an architecture’s cache, is increased. Indeed from (A.21), the arithmetic intensity of the Hadamard products can be found to be given as,

$$\frac{8 \cdot 26 \cdot 64 \cdot b}{2 \cdot (64 \cdot 26 + 8b)} \text{ FLOPs/Accesses}$$

where b is a batch size parameter controlling the number of sets of siblings of target boxes, typically taken to be in the range $b \in [32, 128]$ on modern CPUs, which are considered simultaneously per thread, though must be tuned for the cache availability of a given architecture. Specifically the method is optimised such that its throughput is greatest when the amount of data accessed, shown in the denominator of this estimate, can fit into the L1 cache of a given CPU core. In comparison to our method based on matrix-matrix products for which operational intensity increases as a function of rank, the operational intensity of the FFT-M2L approach is fixed due to its reliance on a Hadamard product.

At runtime, both approaches require memory bound data organisations. Our BLAS-M2L approach requires additional copies of multipole data associated with target boxes via transfer vectors. The FFT-M2L requires a re-organisation of data based on frequency in Fourier space, and the inverse operation at the end of the computation. As these data organisations are both local to a target given box they can be effectively multithreaded as the data involved are non-overlapping in their storage buffers.

The major benefit of the FFT-M2L in comparison to the BLAS-M2L approach are the relatively shorter pre-computation times, as the pre-computation only requires the FFT rather than the expensive SVD approaches for M2L matrices described above in spite of the acceleration of the SVD by the rSVD. We compare the relative costs for a range of accuracies in the final evaluated potential in Tables C.1 and C.3. However, we note that the pre-computation is required only once for a given set of source and target particles, and can be re-used over multiple right hand sides of (1.1) if the input point distribution remains unchanged. An additional benefit of the FFT-M2L approach is that the operation is *exact* for translation invariant kernel functions, and once implemented does not require further tuning tailored to the ranks that arise from specific kernel functions as in our approach. Its major disadvantage in comparison to the BLAS-M2L approach are its reliance on a complex data access pattern and intricate explicit SIMD implementation which is challenging to extend to new architectures, and it is unclear how to make efficient in a GPU context. In contrast BLAS operations are already well optimised in software, and increasingly optimised at a hardware level due to their centrality in neural network applications. Furthermore the FFT-M2L matrices restrict us to considering discretisation where the downward check and upward equivalent surfaces of each target/source box are discretised to the same degree in order to interpret the M2L as a convolution type operation, whereas it has been shown in [5] that taking a greater number of check than equivalent points can increase the stability of the MFS method.

5. Numerical Benchmarks. We test our software on the two CPU architectures listed in Table C.2. The x86 AMD 3790X architecture provides an example of a commodity high performance CPU with a high core count and large cache memory and RAM. This architecture allows us to test the performance of our shared memory optimisations across large numbers of threads on a single node. The ARM Apple M1 Pro architecture though not typically used in HPC benchmarks gives an interesting comparison both in terms of the underlying ISA but additionally of an architecture supporting a large and highly efficient ‘unified memory’ pool with atypically large

cache sizes. Furthermore, it has a core count typical of machines available to the majority of developers. The M1 Pro’s unified memory supports significantly higher computational throughput than the AMD architecture, and allows us to observe the impact of operational intensity on runtimes with respect to the more typical AMD architecture. Interestingly, when using Apple’s Accelerate [4] framework for BLAS operations the M1 Pro makes use of specialised registers for matrix computations, offering an example of an architectural feature which can be automatically exploited by the structure of our algorithm in terms of BLAS operations when using the BLAS-M2L approach. We also note that such specialised matrix registers aren’t unique to Apple’s M Series and are becoming more common also in other CPU architectures.

Our benchmark problem is the evaluation of potentials between 1×10^6 source and target points distributed uniformly in a unit box. Sources and targets are considered to be the same set, with sources assigned random source densities. We approximate error in the evaluated potential with the mean relative error, ε , over all target points with respect to the direct evaluation of the kernel. We identify the best parameter settings for the FMM as those which allow us to achieve a given error of $\mathcal{O}(\varepsilon)$ in the least time. We identify these parameters with a grid-search, the results of which are shown in Tables C.1 and C.3 when using the FFT-M2L and BLAS-M2L approaches respectively.

Interestingly we observe a significant variation in the optimal parameters between both architectures. On the AMD architecture, we are typically able to take shallower trees, often depth $d = 4$ with at most $8^4 = 4096$ leaf boxes, to discretise our benchmark problem, likely due to its higher core-count for which our SIMD based P2P implementation is highly optimised. On the AMD architecture we use OpenBLAS for linear algebra, using Apple Accelerate on the M1 Pro. When using BLAS-M2L this seemingly influences the resulting accuracy of the SVD in single precision, as we are able to achieve significantly greater compression in the M2L operator matrices on the M1 Pro. Furthermore, we note that Apple Accelerate is able to significantly reduce setup times time when using BLAS-M2L in contrast to OpenBLAS, especially at high expansion orders in double precision despite the fewer computational resources of the M1 Pro in comparison to the AMD 3790X.

The runtimes when using BLAS-M2L and FFT-M2L are illustrated in Table 5.1 for the M1 Pro and AMD architectures respectively. We illustrate the corresponding computational throughputs and required storage of the M2L operation when using either BLAS-M2L or FFT-M2L in Table 5.2.

In single precision we don’t observe a significant difference in the best runtimes when using BLAS-M2L and FFT-M2L on either of the architectures tested. However, we notice from Table 5.2 that the FFT-M2L approach rapidly achieves bandwidth saturation when the associated data sizes of the M2L operator matrices is larger than, or comparable in size to, the L2 cache of each architecture. This results in diverging performance for high accuracy experiments in double precision, with the BLAS-M2L outperforming the runtime performance of the FFT-M2L on both architectures tested due to its increasing operational intensity for larger matrix sizes.

The favourable memory architecture of the M1 Pro, as well as its specialised matrix co-processor, make it interesting to see how it handles multiple source density vectors for a given point distribution when using the BLAS-M2L approach. We observe in Table 5.1 the benefit of further increased operational intensity on per-vector end-to-end kiFMM runtimes, especially in single precision when using multiple source density vectors. This is effect is visibly reduced on the AMD architecture, where even in single precision the larger data sizes often lead to deteriorating performance by

increasing the number of source density vectors.

Our experiments imply architecture dependent performance considerations for the kiFMM, for which we identify the following four cases:

- **High Bandwidth, High Core Count:** If an architecture exhibits high bandwidth and high core-counts, both our P2P and BLAS-M2L implementations are favourable, and one can use shallow octrees. Examples include the NVidia Grace CPU Superchip, with a total of 144 ARM v9 cores, with a peak bandwidth of 1 TB/s.
- **Low Bandwidth, High Core Count:** If bandwidth is relatively low, with a high core-count such as the AMD 3790X tested, there is relatively little to discern the BLAS-M2L and FFT-M2L at lower accuracies and especially in single precision. However, the high core-count lends itself to using shallow trees, and a greater reliance on the optimised P2P operation.
- **High Bandwidth, Low Core Count:** If bandwidth is high, with a modest core-count such as the Apple M1 Pro tested, the BLAS-M2L consistently outperforms the FFT-M2L due to its higher operational intensity which grows with matrix size. In this setting one must generally use deeper trees, to account for the relatively poorer performance of our P2P implementation with fewer cores.
- **Low Bandwidth, Low Core Count:** In this case it is likely that the bandwidth constrained effects of the FFT-M2L will not be noticeable, and the BLAS-M2L and FFT-M2L can be used interchangeably, again necessitating deeper trees due to the lower number of cores.

The implications for extending our implementation to a heterogenous setting are that the best performance could be achieved with shallow trees exploiting the efficiency of the BLAS-M2L with the bulk of the potential evaluation conducted using the P2P operation implemented on GPUs. These steps are data independent and can be called asynchronously.

Though not presented at larger problem sizes, we see our results comparing BLAS-M2L and FFT-M2L to hold as larger problems will necessitate deeper trees for which our operational intensity estimates for both methods provided in Appendices A and B still apply.

In Figure 5.1, we evaluate the effectiveness of our approach for computing potentials in scenarios involving a highly non-uniform point distribution. We observe a relatively modest increase in runtime of approximately 44 % in this case compared to a uniform random distribution with the same number of source and target points evaluated to the same level of accuracy in the final potential taken as a baseline. This demonstrates the suitability of our uniform tree implementation for tackling non uniform point distributions arising from the efficiency of our P2P implementation, and memory intensive operations confined to a minimal number of M2L operations.

6. Conclusion. In this paper we have shown that with suitable blocking and careful use of randomised SVDs a BLAS based kiFMM can be competitive with an FFT based kiFMM implementation for problems described by the Laplace kernel. Performance between both methods is dependent on both architecture and the desired accuracy in the evaluated potentials, where for high order and double precision settings our BLAS-M2L approach results in better runtime performance though at the cost of a moderately more expensive setup phase due its reliance on the SVD.

The advantage of our approach is not only that the implementation itself is simpler, but that its high operational intensity is well suited to the architectures of modern

Table 5.1: Mean end-to-end algorithmic (\mathbf{T}_{FMM}), M2L (\mathbf{T}_{M2L}) and P2P (\mathbf{T}_{P2P}) runtimes in milliseconds for achieving a given relative error (ϵ) with both BLAS-M2L and FFT-M2L for our benchmark problem. We report runtimes for the best parameter settings documented in Tables C.1 and C.3. For BLAS based field translations we also report the runtime per source density vector, when the FMM is called multiple times with different source density data for the same source/target point data. The number of source density vectors is given in brackets, and we highlight the fastest mean runtime per FMM call for each relative error. Error on runtimes are reported from the final digit. Results are presented with multithreading enabled, where one logical thread is pinned to each physical core on the architectures tested.

(a) Apple M1 Pro

$\mathcal{O}(\epsilon)$	BLAS-M2L (1)			BLAS-M2L (5)			BLAS-M2L (10)			FFT-M2L		
	\mathbf{T}_{FMM}	\mathbf{T}_{M2L}	\mathbf{T}_{P2P}	\mathbf{T}_{FMM}	\mathbf{T}_{M2L}	\mathbf{T}_{P2P}	\mathbf{T}_{FMM}	\mathbf{T}_{M2L}	\mathbf{T}_{P2P}	\mathbf{T}_{FMM}	\mathbf{T}_{M2L}	\mathbf{T}_{P2P}
Single Precision												
10^{-3}	233	138	81	194	99	84	195	94	85	153	63	78
10^{-4}	232	138	82	196	104	85	189	94	87	242	149	88
Double Precision												
10^{-6}	787	555	160	719	516	170	757	525	174	1094	866	173
10^{-8}	1375	154	1112	1370	137	1164	1365	132	1125	1614	261	1233
10^{-10}	1562	257	1159	1577	224	1139	1556	223	1125	1954	517	1244

(b) AMD 3790X

$\mathcal{O}(\epsilon)$	BLAS-M2L (1)			BLAS-M2L (5)			BLAS-M2L (10)			FFT-M2L		
	\mathbf{T}_{FMM}	\mathbf{T}_{M2L}	\mathbf{T}_{P2P}	\mathbf{T}_{FMM}	\mathbf{T}_{M2L}	\mathbf{T}_{P2P}	\mathbf{T}_{FMM}	\mathbf{T}_{M2L}	\mathbf{T}_{P2P}	\mathbf{T}_{FMM}	\mathbf{T}_{M2L}	\mathbf{T}_{P2P}
Single Precision												
10^{-3}	126	16	109	122	6	110	122	6	110	122	11	110
10^{-4}	130	18	110	131	12	110	134	19	110	152	42	110
Double Precision												
10^{-6}	376	126	222	449	186	223	455	204	224	474	216	221
10^{-8}	542	277	222	651	367	223	666	394	223	733	465	221
10^{-10}	844	538	220	973	650	220	991	699	221	1240	937	221

hardwares, which are increasingly implemented with hardware optimisations prioritising BLAS operations. Furthermore, our implementation naturally extends itself to porting to batched-BLAS implementations on GPUs, though latency and memory copy operations need to be carefully tuned for here. BLAS-M2L operators also naturally extend to treating many FMM charges at the same time, giving potential for additional cache reuse on architectures with favourable bandwidth properties as the M1 Pro tested in this work.

The main trade-off in addition to the relatively longer setup time are more sources of error in the evaluated potential as a result, due to the sensitivity of this compression on the properties of the kernel being evaluated. Given that emerging hardware architectures, both CPU and GPU, are likely to contain significant software and hardware optimisations for BLAS operations the importance of developing algorithm implementations which take advantage of this development will continue to grow.

Acknowledgments. We are grateful to Matthew Scroggs for his valuable assistance in software development during this research, as well as Dhairya Malhotra for interesting and insightful conversations regarding PVFMM.

Table 5.2: Throughput and required storage of data associated with the M2L operator when using BLAS-M2L or FFT-M2L. We observe that the throughput of the BLAS-M2L method in single precision is low until the associated data sizes are large enough to fully utilise available cache, at which point the fixed costs of setting up the calculation are amortised and we observe high throughputs which increase with accuracy and hence data sizes. We observe that the data associated with the FFT-M2L approach is always larger than the BLAS-M2L, and as such we always operate at the bandwidth limit of the method - which saturates at approximately 120 GFLOP/s in single precision and 60 GFLOP/s in double precision for the M1 Pro, and 80 GFLOP/s in single precision and 40 GFLOP/s in double precision for the AMD architecture.

(a) Apple M1 Pro

$\mathcal{O}(\epsilon)$	M2L Throughput (GFLOP/s)		M2L Storage (MB)	
	BLAS-M2L	FFT-M2L	BLAS-M2L	FFT-M2L
Single Precision				
10^{-3}	3	114	0.1	3.7
10^{-4}	11	110	0.2	8.1
Double Precision				
10^{-6}	91	63	4.4	51
10^{-8}	109	63	12.7	117.0
10^{-10}	179	63	33.9	223.4

(b) AMD 3790X

$\mathcal{O}(\epsilon)$	M2L Throughput (GFLOP/s)		M2L Storage (MB)	
	BLAS-M2L	FFT-M2L	BLAS-M2L	FFT-M2L
Single Precision				
10^{-3}	25	81	0.2	3.7
10^{-4}	84	47	0.1	8.1
Double Precision				
10^{-6}	69	31	4.4	51.2
10^{-8}	64	35	12.7	117.0
10^{-10}	108	35	33.9	223.4

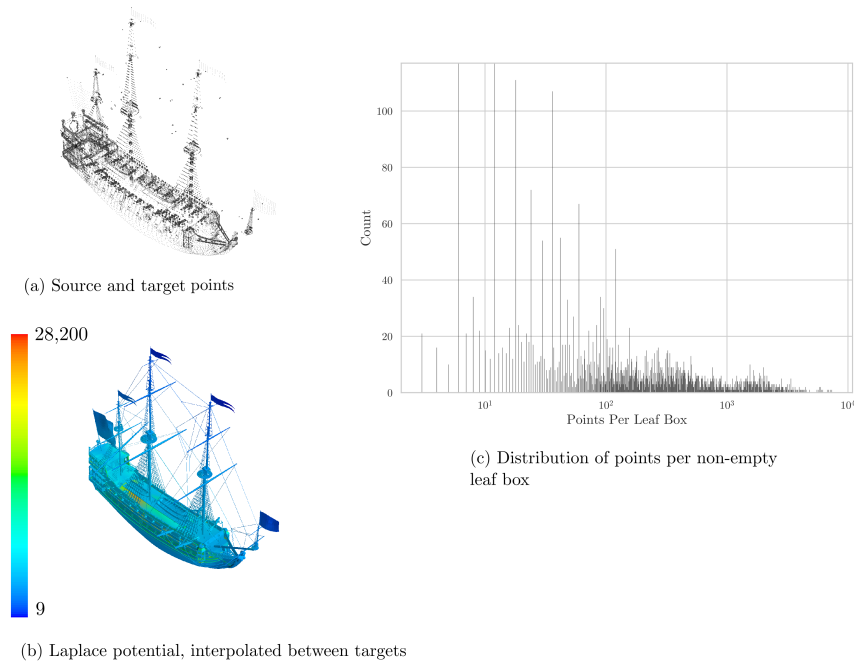


Fig. 5.1: The Laplace potential computed such that the mean relative error of the potential evaluated at all target points is $\mathcal{O}(\epsilon) = 10^{-10}$ using FFT-M2L with expansion order $P = 10$ and block size set to 16 on the AMD 3790X architecture. The experiment is run on a highly-non uniform point distribution consisting of the 1,441,572 vertices of 480,524 triangles each with a random source density using a uniformly refined octree, refined to a depth of $d = 6$, containing 8192 non-empty leaf boxes. Here we take the source and target points to be the same set. The mean runtime was found to be 5455 s where error is reported from the last digit. Computing the potential for an equivalent number of uniformly distributed source/target points we find the mean runtime to be 3798 ms which we can take to be a baseline level of performance, implying that the non-uniformity resulted in an approximately $\sim 44\%$ greater runtime. The histogram illustrates the highly non-uniform point distribution, with leaf boxes containing anywhere between 1 and 10^4 points. The geometry is provided by [8]. Results are presented with multithreading enabled, where one logical thread is pinned to each physical core on the architectures tested.

Appendix A. The FFT M2L Algorithm.

A.1. Algorithm. We review the method introduced in [23] and re-implemented in [31] for maximising the arithmetic intensity of the evaluation of check potentials (2.4) using the FFT below. We use the case of a one dimensional problem for clarity.

For an order P multipole or local expansion, we described a check or equivalent surface as consisting of P evenly spaced points along each axis as shown in Figure 2.1 in three dimensions. In one dimension, this would correspond to a line shown in Figure A.2. We define the *convolution grid* as an embedding of this surface into a grid defined by $\tilde{P} = 2P$ points along each axis through its volume, that encloses the grid describing the equivalent surface, which we call the *surface grid*, and is aligned at a given corner of the surface grid. In three dimensions the convolution grid is instead a cube evenly discretised by \tilde{P} points along each axis. We thus note that the convolution grid consists of \tilde{P}^d points in dimension d .

We define a sequence of kernel evaluations as

$$K_j = K(x_c, \tilde{y}_j),$$

where x_c is a chosen point on the target check surface and \tilde{y}_j are points on the convolution grid as shown in Figure A.2. This sequence captures all the unique kernel evaluations between the points discretising the source and target boxes. In the case of Figure A.2, we choose $x_c = x_0$ and construct a sequence

$$K[j] = \begin{cases} K(x_c, \tilde{y}_{j+1}), & j = 0, \dots, 2P - 2 \\ 0, & j = 2P - 1, \end{cases}$$

where we use zero padding to handle the circular shift. We also define a sequence of densities on the convolution grid, defined through our embedding of the surface grid, placing zeros where densities from the surface grid are not mapped,

$$\tilde{q}[j] = \begin{cases} 0, & j = 0, 1 \dots P - 1, \\ q[j - P], & j = P, \dots, 2P - 1, \end{cases}$$

where $q[i]$, $i = 0, \dots, P - 1$, is the original sequence of densities on the surface grid.

We compute the check potential as a convolution of the flipped sequence $K'[2P - 1 - i] = K[i]$ with the source densities placed on the convolution grid

$$\phi[i] = \sum_{j=0}^{2P-1} \tilde{q}[j] K'[(i - j)_{2P}]$$

where $\phi[i]$ is the potential at $\phi(x_i)$.

Computed for a given box σ , finding the check potential consists of mapping the sequence of densities to the convolution grid corresponding to the multipole expansions for each box A in its interaction list I_σ , computing the Discrete Fourier Transform (DFT) of this sequence and computing the Hadamard product with the result with the DFT of the flipped sequence of kernel evaluations corresponding to that particular relative position between source and target box which can potentially be precomputed and cached. The DFT is accelerated with the FFT, however the component wise

Hadamard product is of low operational intensity as each item of both sequence is used once per each required read and write operations.

S_1^1	S_2^1	S_1^2	S_2^2	S_1^3	S_2^3
S_3^1	S_4^1	S_3^2	S_4^2	S_3^3	S_4^3
S_1^4	S_2^4	T_1	T_2	S_1^4	S_2^4
S_3^4	S_4^4	T_3	T_4	S_3^4	S_4^4
S_1^5	S_2^5	S_1^6	S_2^6	S_1^5	S_2^5
S_3^5	S_4^5	S_3^6	S_4^6	S_3^5	S_4^5

The source clusters (S_i^j) where i is the index of the source cluster and j is the index of each source box within a source cluster, for a target cluster (T_j) where j is the index of each target box within the target cluster.

Fig. A.1: Source and target clusters illustrated in two dimensions. Here a target cluster consisting of four sibling quadrants is shown in ping, and the eight source clusters, which consist of the target cluster's parent's neighbours are shown in blue.

In three dimensions, this is an $O(\tilde{P}^3)$ operation which requires $O(\tilde{P}^3)$ memory accesses. For this case the authors of [23] improve the arithmetic intensity by considering the interaction of eight source siblings with eight target siblings, allowing for efficient vectorisation. eight siblings together are referred to as a 'cluster'. All the M2L translations for a target cluster will occur with boxes that are children of the neighbours of the cluster's shared parent, termed *source clusters*. We illustrate this in two dimensions in Figure A.1. In two dimensions the source clusters form a halo consisting of eight clusters, around each target cluster. In three dimensions this halo consists of 26 source clusters. In two dimensions, there are 16 unique interaction pairs of source and target boxes between a given source cluster and a target cluster, correspondingly in three dimensions there are 64 such interactions. Thus each source and target cluster will have 64 corresponding sequences of Fourier coefficients of kernel evaluations $K^{(i)}$ of length $\hat{P} = \tilde{P}^3$, where i indexes the interaction between a source and target box contained in the source/target clusters being considered. Writing the sequences in order we have,

$$\begin{aligned}
 [K^{(1)}, K^{(2)}, \dots, K^{(64)}] = & \\
 & [[K^{(1)}[0], K^{(1)}[1], \dots, K^{(1)}[\hat{P} - 1]], \\
 & [K^{(2)}[0], K^{(2)}[1], \dots, K^{(2)}[\hat{P} - 1]], \\
 & \dots, \\
 & [K^{(64)}[0], K^{(64)}[1], \dots, K^{(64)}[\hat{P} - 1]],
 \end{aligned}$$

where the index in brackets is the Fourier frequency. These sequences are permuted into *frequency order*,

$$\begin{aligned}
 (A.1) \quad & [[K^{(1)}[0], K^{(2)}[0], \dots, K^{(64)}[0]], \\
 & [K^{(1)}[1], K^{(2)}[1], \dots, K^{(64)}[1]], \\
 & \dots, \\
 & [K^{(1)}[\hat{P} - 1], K^{(2)}[\hat{P} - 1], \dots, K^{(64)}[\hat{P} - 1]]
 \end{aligned}$$

The Fourier coefficients \hat{q} of the multipoles are ordered similarly. Consider the Fourier coefficients of a source cluster consisting of eight source boxes.

$$\begin{aligned}
\text{(A.2)} \quad & [\hat{q}^{(1)}, \hat{q}^{(2)}, \dots, \hat{q}^{(8)}] = \\
\text{(A.3)} \quad & [[\hat{q}^{(1)}[0], \dots, \hat{q}^{(1)}[\hat{P} - 1]], \\
\text{(A.4)} \quad & [\hat{q}^{(2)}[0], \dots, \hat{q}^{(2)}[\hat{P} - 1]] \\
& \dots \\
\text{(A.5)} \quad & [\hat{q}^{(8)}[0], \dots, \hat{q}^{(8)}[\hat{P} - 1]]
\end{aligned}$$

These are also permuted into frequency order,

$$\begin{aligned}
\text{(A.6)} \quad & [[\hat{q}^{(1)}[0], \hat{q}^{(2)}[0], \dots, \hat{q}^{(8)}[0]], \\
\text{(A.7)} \quad & [\hat{q}^{(1)}[1], \hat{q}^{(2)}[1], \dots, \hat{q}^{(8)}[1]] \\
& \dots \\
\text{(A.8)} \quad & [\hat{q}^{(1)}[\hat{P} - 1], \hat{q}^{(2)}[\hat{P} - 1], \dots, \hat{q}^{(8)}[\hat{P} - 1]]
\end{aligned}$$

The Hadamard product computation for the k 'th frequency component of the check potential in Fourier space is then written as an 8×8 operation between all source boxes in an 8-cluster with the corresponding target boxes in an 8-cluster, where each element in a sequence is computed as,

$$\text{(A.9)} \quad \hat{\phi}^{(i)}[k] = K^{(i+8j)}[k] \cdot \hat{q}^{(i)}[k] + \hat{\phi}^{(i)}[k]$$

where $i, j \in [1, 8]$ and the sequence $\hat{\phi}^{(i)}[\cdot]$ corresponds to the check potential in Fourier space. The resulting sequence of check potentials in Fourier space is now in frequency order, and arranged by target cluster

$$\begin{aligned}
\text{(A.10)} \quad & [[\hat{\phi}^{(1)}[0], \hat{\phi}^{(2)}[0], \dots, \hat{\phi}^{(8)}[0]], \\
\text{(A.11)} \quad & [\hat{\phi}^{(1)}[1], \hat{\phi}^{(2)}[1], \dots, \hat{\phi}^{(8)}[1]] \\
& \dots \\
\text{(A.12)} \quad & [\hat{\phi}^{(1)}[\hat{P} - 1], \hat{\phi}^{(2)}[\hat{P} - 1], \dots, \hat{\phi}^{(8)}[\hat{P} - 1]]
\end{aligned}$$

These must be de-interleaved such that

$$\begin{aligned}
\text{(A.13)} \quad & [[\hat{\phi}^{(1)}[0], \hat{\phi}^{(1)}[1], \dots, \hat{\phi}^{(1)}[\hat{P} - 1]], \\
\text{(A.14)} \quad & [\hat{\phi}^{(2)}[0], \hat{\phi}^{(2)}[1], \dots, \hat{\phi}^{(2)}[\hat{P} - 1]] \\
& \dots \\
\text{(A.15)} \quad & [\hat{\phi}^{(8)}[0], \hat{\phi}^{(8)}[2], \dots, \hat{\phi}^{(8)}[\hat{P} - 1]]
\end{aligned}$$

for each target cluster, at which point an inverse DFT can be computed over the above sequences to recover the check potential.

The algorithm for problems in three dimensions for computing check potentials at each level $l \in [2, d]$ during the downward pass of the kiFMM consists of:

1. In a pre-computation step, compute sequences of kernel evaluations $K[\cdot]$ corresponding to all unique relative positions between a target cluster and source clusters in its halo. These are appropriately padded, and the FFT is computed for each one. The resulting sequences are then permuted into frequency order. Depending on the properties of the kernel, they can be stored once and scaled per level $l \in [2, d]$ in an octree, or must be stored for each level, $l \in [2, d]$, in an octree.
2. First placing the multipole data for each source box on the convolution grid, compute the FFT of all multipole data at this level.
3. Interleave the Fourier coefficients of the transformed multipole data for sets of sibling source boxes into frequency order.
4. For each frequency, indexed by $k \in [0, \hat{P} - 1]$, loop over all 26 source clusters in each target cluster’s halo. For each source cluster, perform an 8×8 operation for the Hadamard product for the Fourier coefficients of the check potentials of each target cluster. Each element in the Hadamard product is computed with (A.9).
5. De-interleave the Fourier coefficients of the check potentials at each target cluster.
6. Compute the inverse FFT to recover the check potentials for each target cluster.

A.2. Optimisation. Steps 2, 3 and 5 contain significant data organisation which must be done at runtime, and are therefore memory bound. However, as data associated with each box does not overlap these steps can be effectively parallelised with multithreading.

Additionally, Step 4 in the above algorithm can be effectively multithreaded over each frequency $k \in [0, \hat{P} - 1]$. Each thread is then responsible for computing all the Hadamard products for all target clusters due to the source clusters in their halos at the k ’th frequency. Threads are then pinned to cores for data locality.

In order to achieve high computational throughput the authors suggest that *blocks* of target clusters should be taken such that the L1 cache of each core is filled [22]. With this, all source cluster directions are looped over for an entire block for the k ’th frequency components by each thread. For the architectures listed in Table (C.2) we find good performance with block sizes of between 32 and 128 target clusters.

A drawback of this approach to M2L involves computing *all* translation directions for all source clusters relative to a target cluster, even if they do not appear in the interaction list of a target box in the target cluster. In this case the corresponding sequence of Fourier transformed kernel evaluations is replaced with zeros. This strategy therefore introduces some redundant computations, approximately $\sim 10\%$ according to the original authors [22], however this is worthwhile given the increased computational throughput.

Depending on the properties of the kernel, we can pre-compute and potentially scale the matrices corresponding to (A.1) for all 26 relative positions between source and target clusters in 3 dimensions at each level l . Additionally, for sequences of kernel evaluations that correspond to real numbers, such as for (1.2), the size of the resulting sequence of Fourier coefficients can be halved.

In order to further improve computational throughput, the original authors use explicit SIMD intrinsics for x86 architectures for the implementation of the 8×8 Hadamard product during the calculation in the parallel loop, as the sizes are too small to justify a BLAS call and autovectorisers struggle to optimise the complex multiply add

operations required on x86. In our implementation we follow the recommendations of the Intel architecture reference for this operation for AVX and AVX2 instruction sets [20]. For Arm architectures, we use NEON FCMA instructions, which contain special intrinsics for performing fused complex multiply and add operations. Our software also contains a generic autovectorised implementation, allowing our codes to run on common hardware targets supported by Rust’s LLVM based compiler.

The frequency re-ordering together with reformulation as small efficient 8×8 Hadamard products is key to make the method have high computational throughput. However, the permutations required to form and handle the frequency ordering results in practice in a complex code structure and care needs to be taken to do the re-ordering efficiently for it not to dominate execution time. In [23] this was achieved by re-ordering mutable references to the actual data in a multithreaded loop. Instead in our implementation we allocate new buffers to store the re-ordered data, which we can then iterate over in chunks corresponding to each frequency, and post-process the frequency ordered results for check potential back into Morton order.

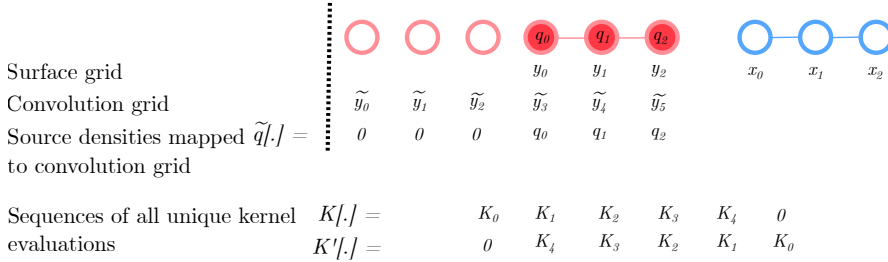


Fig. A.2: We show a one dimensional M2L translation for $p = 3$ expansions from the red source box $\{y_j\}_{j=0}^2$, embedded in a convolution grid $\{\tilde{y}_j\}_{j=0}^{2P-1}$, with associated multipole expansion coefficients $\{q_j\}_{j=0}^2$ to a blue target box $\{x_i\}_{i=0}^2$. We associate the required sequences of kernel evaluations $K[\cdot]$, and the flipped sequence $K'[\cdot]$, and the sequence of source densities $\tilde{q}[\cdot]$ associated with points on the convolution grid

A.3. Analysis. As with our BLAS-M2L, the most challenging part of data access is ensuring the lookups required during the M2L for each box’s interaction list, I_σ , are contiguous. The multipole data in the halo of each target box is stored in a single contiguous buffer, in Morton order, over the source boxes at a given level. For each target box, we calculate its halo, and use a technique of index pointers to look up required data, whereby we store together the index position of the start of each multipole/local data for a given box within the global buffer storing all multipole/local data with its associated Morton key. Using index pointers, we create references to the multipole data of each target box’s halo stored in frequency order. Therefore in the parallel loop we must lookup each reference in a loop over the halo data, and accumulate in a global buffer containing the check potentials for all target boxes, stored in frequency order and Morton order, un-permuting the check potentials from frequency order as a post-processing step. Similarly to our BLAS-M2L approach, the halo of each target box is calculated as a pre-processing step, and removes the need to explicitly construct and process interaction lists by indexing the octree at runtime. Efficient cache usage is achieved in this method by processing the halos of multiple target clusters at once for each frequency.

In our analysis we assume a uniformly refined tree such that the number of source

boxes, N_σ , and the number of target boxes, N_τ at a given level $l \in [0, d]$ of an octree of depth d are equal to $N_\sigma = N_\tau = 8^l$.

As Step 1 in the above algorithm can be done as a pre-computation it does not enter our analysis for the runtime cost of this approach. In Step 2, we must place all multipole data for each source box on the convolution grid. In the MFS in three dimensions the check and equivalent surfaces are discretised with

$$(A.16) \quad 6 \cdot (P - 1)^2 + 2$$

points, this step therefore requires $\mathcal{O}(8^l \cdot P^2)$ read, addition and save operations, resulting in an operational intensity of

$$(A.17) \quad \frac{1}{2} \text{ FLOPs/Accesses.}$$

The achieved operational intensity of the FFT in Step 2 is dependent both on the exact implementation of the operation to take advantage of Instruction Level Parallelism (ILP) optimisations, but also on the radix taken for the algorithm and the size of the data. From [25] operational intensity of this step can be estimated as

$$(A.18) \quad \mathcal{O}(\log_2(P)) \text{ FLOPs/Accesses,}$$

where we estimate the intensity for a radix of two in the FFT. In Step 3, we must interleave the Fourier coefficients of the transformed multipole data for sets of sibling source boxes into frequency order. This involves $\mathcal{O}(8^l \cdot \hat{P})$ read, addition and save operations, resulting in an operational intensity of

$$(A.19) \quad \frac{1}{2} \text{ FLOPs/Accesses.}$$

Step 4 involves the Hadamard product, naively computed this results in an operational intensity of $\mathcal{O}(1)$. In the scheme presented above, we are required to load $64 \cdot 26$ entries corresponding to the transformed kernel evaluations for the halo source boxes with respect to a target box from main memory. In addition to the loading of $\mathcal{O}(8^l \cdot \hat{P}^3)$ entries corresponding to the Fourier transformed multipole data in each source cluster, the Hadamard products result in $\mathcal{O}(26 \cdot 64 \cdot 8^{l-1} \hat{P}^3)$ multiplication and addition operations over all target clusters at level l . These multiplications involve complex numbers, therefore each require a total of four multiplication and four addition operations to accumulate the result. Finally we require $\mathcal{O}(8^l \cdot \hat{P}^3)$ saves to store the resulting Fourier coefficients of check potentials. This results in an estimated operational intensity bounded by,

$$(A.20) \quad \frac{8 \cdot 26 \cdot 64 \cdot 8^{l-1} \hat{P}^3}{2 \cdot (64 \cdot 26 + 2 \cdot 8^l \cdot \hat{P}^3)} \text{ FLOPs/Accesses}$$

where the additional factor of two in the denominator comes from the fact that the data are complex numbers.

The *arithmetic intensity*, which instead measures the ratio of FLOPs to memory traffic from CPU cache rather than main memory is a function of L1 cache size in the above algorithm. In Step 4 we load a batch, σ , of eight Fourier coefficients corresponding to each of $k \in [0, \hat{P} - 1]$ frequencies into the L1 cache of each CPU core, resulting in $64 \cdot 26$ loads for the Fourier coefficients of the kernel evaluations and $8b$ saves per CPU core to save the check potentials data after Hadamard product. Each core then executes $26 \cdot 64 \cdot b$ multiplication and addition operations for each batch. This results in an arithmetic intensity bounded by,

$$(A.21) \quad \frac{8 \cdot 26 \cdot 64 \cdot b}{2 \cdot (64 \cdot 26 + 8b)} \text{ FLOPs/Accesses}$$

per batch b where again we notice that the data involved are complex numbers, assuming that the data of size $64 \cdot 26 + 8b$ entries, fits into the L1 cache of each core. We observe that while the operational intensity indicates that this step is memory bound, the observed throughput is high due to the fact that arithmetic intensity is an increasing function of L1 cache size. In the original presentation they report that up to 50 % of theoretical peak performance is achieved on their tested 16 core Intel Xeon E5-2680 architectures with optimal choice of batch size $b = 128$ with the additional use of explicit SIMD and FMA instructions to perform the complex multiplications [22]. On x86 architectures the complex multiplications involve shuffle operations which reduces the achieved throughput.

Step 5 performs a de-interleaving operation, similar to Step 2, and therefore also results in an operational intensity of

$$(A.22) \quad \frac{1}{2} \text{ FLOPs/Accesses}$$

Similarly, the inverse FFT results in an operational intensity of

$$(A.23) \quad \mathcal{O}(\log_2(P)) \text{ FLOPs/Accesses}$$

Appendix B. BLAS-M2L Algorithm Analysis.

Consider the following matrix-matrix multiplication and accumulation operation for real matrices, such as M2L matrices that arise from the Laplace kernel (1.2)

$$(B.1) \quad \mathbf{C}_{M \times N} = \mathbf{A}_{M \times K} \times \mathbf{B}_{K \times N} + \mathbf{C}_{M \times N}$$

where $\mathbf{C} \in \mathbb{R}^{M \times N}$, $\mathbf{A} \in \mathbb{R}^{M \times K}$, $\mathbf{B} \in \mathbb{R}^{K \times N}$.

Each element in (B.1) is calculated as $\mathbf{C}_{ij} = \sum_{l=1}^K \mathbf{A}_{il} \mathbf{B}_{lj} + \mathbf{C}_{ij}$. In total this requires K multiply and $K - 1$ addition operations per element in the sum and 1 more addition for the accumulation into \mathbf{C} , resulting in $M \cdot N \cdot 2K$ FLOPs in total. The total number of accesses from memory involve reading \mathbf{A} and \mathbf{B} and reading and writing to \mathbf{C} , resulting in $M \cdot K + K \cdot N + 2 \cdot M \cdot N$ accesses.

This gives an estimate for the operational intensity of

$$(B.2) \quad \frac{2 \cdot M \cdot N \cdot K}{M \cdot K + K \cdot N + 2 \cdot M \cdot N} \text{ FLOPs/Accesses}$$

Most modern CPU and GPU architectures support Fused Multiply and Add (FMA) instructions, which can effectively compute the multiply and add operations in a single instruction, with the cost of a single multiply operation. This leads to an approximate doubling of the throughput in the above estimates through an architecture, without increasing memory traffic.

In our analysis we assume a uniformly refined tree such that the number of source boxes, N_σ , and the number of target boxes, N_τ at a given level $l \in [0, d]$ of an octree of depth d are equal to $N_\sigma = N_\tau = 8^l$.

As Step 1 can be performed as a pre-computation it does not enter the runtime complexity estimate of the algorithm. In Step 2, we compute the compressed multipole expansions by applying \mathbf{S}^T to a buffer containing all the multipole expansions at a given level l , which are stored contiguously in our implementation. As these correspond to real matrix-matrix multiplications, this results in an operational intensity of

$$\frac{2 \cdot 8^l \cdot k \cdot N_{\text{equiv}}}{2 \cdot 8^l \cdot k + N_{\text{equiv}} \cdot k + 8^l \cdot N_{\text{equiv}}} \text{ FLOPs/Accesses}$$

In Step 3, we are required to access and store the compressed multipole expansions associated with up to N_i source boxes associated with each transfer vector as $i \in [1, 316]$. We can obtain an upper bound for this cost by assuming that *every* source box at level l appears once in each buffer, i.e. $N_i = N_\sigma = 8^l$ for all $i \in [1, 316]$.

This is true for all *interior boxes* which we define as boxes which located at 3 box widths away from the boundary of the domain defined by the octree. We illustrate interior boxes in Figure B.1. These boxes can be associated with any transfer vector $i \in [1, 316]$. With increasing tree level, l , interior boxes grow as $(2^l - 6)^3$ and thus dominate the total number of boxes given by 8^l .

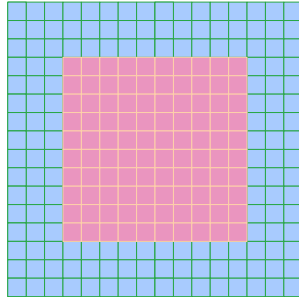


Fig. B.1: Interior boxes illustrated in pink in \mathbb{R}^2 for clarity, for a quadtree discretised to level $l = 4$. Interior boxes increasingly dominate the total number of boxes with increasing tree level.

With this assumption, we require $\mathcal{O}(316 \cdot 8^l \cdot k)$ read operations for all the compressed multipole expansions, $\mathcal{O}(316 \cdot 8^l \cdot k)$ addition operations for accumulating the multipole data and $\mathcal{O}(316 \cdot 8^l \cdot k)$ store operations to save the multipole data to the new buffers. This results in an operational intensity of

$$(B.3) \quad \frac{1}{2} \text{ FLOPs/Accesses}$$

where we observe that this step is memory bound.

In Step 4 we compute the compressed check potentials over a loop of all the transfer vectors. For each transfer vector $i \in [1, 316]$, by the result (B.2) for real matrix-matrix multiplication, this results in an operational intensity of,

$$(B.4) \quad \frac{2 \cdot 8^l \cdot k \cdot k_t}{8^l \cdot k + k_t \cdot k + 2 \cdot 8^l \cdot k_t} + \frac{2 \cdot 8^l \cdot k \cdot k_t}{8^l \cdot k_t + k_t \cdot k + 2 \cdot 8^l \cdot k} \text{ FLOPs/Accesses}$$

where we've used the re-compressed form of \mathbf{C}_t with (3.4). This estimate is the worst case in which the intermediate result has to be accessed from main memory.

In Step 5, we need to accumulate compressed check potentials in buffers associated with each target box at level l . We can obtain an upper bound for this cost by assuming that the interaction lists of each target box is full, i.e. they are each $|I_\tau| = 189$. In which case we require $\mathcal{O}(189 \cdot 8^l \cdot k)$ read operations to lookup the compressed check potentials, $\mathcal{O}(189 \cdot 8^l \cdot k)$ addition operations for accumulating the compressed check potential data and $\mathcal{O}(189 \cdot 8^l \cdot k)$ store operations to save the compressed check potential data to the new buffers. This results in an operational intensity of

$$(B.5) \quad \frac{1}{2} \text{ FLOPs/Accesses}$$

which we again observe is memory bound.

Finally, in Step 6, we calculate the uncompressed check potentials from the compressed form using a matrix-matrix multiplication. Again noticing that these correspond to real matrix-matrix products we see that this results in an operational intensity of,

$$(B.6) \quad \frac{2 \cdot 8^l \cdot N_{\text{check}} \cdot k}{N_{\text{check}} \cdot k + 8^l \cdot k + 2 \cdot 8^l \cdot N_{\text{check}}} \text{ FLOPs/Accesses}$$

Appendix C. Hardware and Software Parameters.

We document the optimal parameters that minimise runtimes found using a grid search for both BLAS and FFT based field translations for the Laplace kernel (1.2) for our benchmarks presented in Table 5.1.

Table C.1 shows the optimal parameters when using FFT-M2L. It shows the tree depth, d , equivalent surface order (which is the same as the check surface order for this method), P_e , the block sizes of the number of target clusters when used when processing multiple target clusters during the parallel loop over frequencies, B and the setup time. Table C.3 shows the optimal parameters when using the BLAS-M2L. It shows the tree depth, d , equivalent surface order, P_e , check surface order, P_c , the number of oversamples in the 'one shot' randomised SVD, N_{over} , as well as the threshold used to cutoff singular values during the compression step, σ_{min} and the setup time.

Table C.1: Optimal parameters for achieving a relative error of $\mathcal{O}(\varepsilon)$ when using the FFT-M2L for the Laplace kiFMM when running our benchmark problem with 1×10^6 source and target points distributed in a unit box. P_e is the expansion order used to construct the equivalent surface, ‘Block Size’ relates to the data brought into L1 cache by each thread and is described in Appendix A.

(a) Apple M1 Pro

$\mathcal{O}(\varepsilon)$	P_e	Block Size	Tree Depth (d)	Setup Time (ms)
Single Precision				
10^{-3}	3	64	5	2013
10^{-4}	4	32	5	1768
Double Precision				
10^{-6}	6	32	5	2053
10^{-8}	8	64	4	2067
10^{-10}	10	32	4	3476

(b) AMD 3790X

$\mathcal{O}(\varepsilon)$	P_e	Block Size	Tree Depth (d)	Setup Time (ms)
Single Precision				
10^{-3}	3	128	4	1187
10^{-4}	4	16	4	1152
Double Precision				
10^{-6}	6	32	4	1628
10^{-8}	8	64	4	2040
10^{-10}	10	32	4	3485

Table C.2: Hardware and software used in our benchmarks, for the Apple M1 Pro we report only the specifications of its ‘performance’ CPU cores. We report per core cache sizes for L1/L2 and total cache size for L3. We note that the Apple M series of processors are designed with unusually large cache sizes, as well as unified memory architectures enabling rapid data access across specialised hardware units such as the performance CPU cores and the specialised matrix coprocessor used for BLAS operations when run with Apple’s Accelerate framework [4].

	Apple M1 Pro	AMD 3790X
Cache Line Size	128 B	64 B
L1i/L1d	192/128 KB	32/32 KB
L2	12 MB	512 KB
L3	24 MB	134 MB
Memory	16 GB	252 GB
Max Clock Speed	3.2 GHz	3.7 GHz
Memory Bandwidth	200 GB/s	102 GB/s
Sockets/Cores/Threads	1/8/8	1/32/64
Architecture	ArmV8.5	x86
SIMD Extensions	Neon	SSE, SSE2, AVX, AVX2
BLAS	Apple Accelerate	Open BLAS
LAPACK	Apple Accelerate	Open BLAS
FFT	FFTW	FFTW
Threading	Rayon	Rayon

Table C.3: Optimal parameters for achieving a relative error of $\mathcal{O}(\epsilon)$ when using BLAS-M2L for the Laplace kIFMM when running our benchmark problem with 1×10^6 uniformly distributed source and target points in a unit box. P_e is the expansion order used to construct the equivalent surface, P_c is the expansion order used to construct the check surface. The ‘Singular Value Threshold’, is the threshold below which associated singular values and vectors of the M2L matrices are filtered out, and ‘M2L compression’ describes the reduction in size of the M2L operator matrices with respect to no thresholding being applied. Oversamples describes the number of oversamples used in the rSVD applied to the M2L operator matrices

(a) Apple M1 Pro

$\mathcal{O}(\epsilon)$	P_e	P_c	Singular Value Threshold	M2L Compression	Oversamples	Tree Depth (d)	Setup Time (ms)
Single Precision							
10^{-3}	3	4	1×10^{-1}	85 %	5	5	1754
10^{-4}	3	4	1×10^{-3}	59 %	10	5	1874
Double Precision							
10^{-6}	5	1	1×10^{-5}	60 %	5	5	2638
10^{-8}	7	7	1×10^{-5}	86 %	10	4	4953
10^{-10}	9	11	1×10^{-7}	84 %	10	4	15499

(b) AMD 3790X

$\mathcal{O}(\epsilon)$	P_e	P_c	Singular Value Threshold	M2L Compression	Oversamples	Tree Depth (d)	Setup Time (ms)
Single Precision							
10^{-3}	3	3	1×10^{-5}	3 %	10	4	668
10^{-4}	3	4	None	0 %	5	4	593
Double Precision							
10^{-6}	5	6	1×10^{-5}	69 %	5	5	2307
10^{-8}	7	9	1×10^{-5}	86 %	10	4	10286
10^{-10}	9	11	1×10^{-7}	84 %	10	4	31795

REFERENCES

- [1] *OpenBLAS: An optimized BLAS library*, 2024, <https://www.openblas.net/>. Accessed: 2024-06-13.
- [2] E. AGULLO, B. BRAMAS, O. COULAUD, E. DARVE, M. MESSNER, AND T. TAKAHASHI, *Task-based fmm for multicore architectures*, SIAM Journal on Scientific Computing, 36 (2014), pp. C66–C93.
- [3] S. AMBIKASARAN, M. O’NEIL, AND K. R. SINGH, *Fast symmetric factorization of hierarchical matrices with applications*, arXiv preprint arXiv:1405.0223, (2014).
- [4] APPLE INCORPORATED, *Accelerate Framework*, 2024, <https://developer.apple.com/documentation/accelerate>. Accessed: 2024-06-13.
- [5] A. H. BARNETT AND T. BETCKE, *Stability and convergence of the method of fundamental solutions for helmholtz problems on analytic domains*, Journal of Computational Physics, 227 (2008), pp. 7003–7026.
- [6] T. BETCKE, M. SCROGGS, AND S. KAILASA, *Green kernels - a rust library for the evaluation of green’s function kernels*. <https://github.com/bempp/green-kernels>, 2024. Accessed: 2024-06-17.
- [7] P. BLANCHARD, B. BRAMAS, O. COULAUD, E. DARVE, L. DUPUY, A. ETCHEVERRY, AND G. SYLVAND, *Scalfmm: A generic parallel fast multipole library*, in SIAM Conference on Computational Science and Engineering (SIAM CSE 2015), 2015.
- [8] BOLBOT, *Old ship*. Thingiverse, 2018, <https://www.thingiverse.com/thing:3253610>. Accessed: 2024-07-10.
- [9] B. BRAMAS, *Tbmm: A c++ generic and parallel fast multipole method library*, Journal of Open Source Software, 5 (2020), p. 2444.
- [10] A. CABRERA, S. HITEFIELD, J. KIM, S. LEE, N. R. MINISKAR, AND J. S. VETTER, *Toward performance portable programming for heterogeneous systems on a chip: A case study with qualcomm snapdragon soc*, in 2021 IEEE High Performance Extreme Computing Conference (HPEC), IEEE, 2021, pp. 1–7.
- [11] A. CHANDRAMOWLISHWARANY, K. MADDURI, AND R. VUDUC, *Diagnosis, tuning, and redesign for multicore performance: A case study of the fast multipole method*, in SC’10: Proceedings of the 2010 ACM/IEEE International Conference for High Performance Computing, Networking, Storage and Analysis, IEEE, 2010, pp. 1–12.
- [12] O. COULAUD, P. FORTIN, AND J. ROMAN, *High performance blas formulation of the multipole-to-local operator in the fast multipole method*, Journal of Computational Physics, 227 (2008), pp. 1836–1862.
- [13] O. COULAUD, P. FORTIN, AND J. ROMAN, *High performance blas formulation of the adaptive fast multipole method*, Mathematical and Computer Modelling, 51 (2010), pp. 177–188.
- [14] J. DONGARRA, S. TOMOV, P. LUSZCZEK, J. KURZAK, M. GATES, I. YAMAZAKI, H. ANZT, A. HAIDAR, AND A. ABDELFAH, *With extreme computing, the rules have changed*, Computing in Science & Engineering, 19 (2017), pp. 52–62.
- [15] W. FONG AND E. DARVE, *The black-box fast multipole method*, Journal of Computational Physics, 228 (2009), pp. 8712–8725.
- [16] H. FUJIWARA, *The fast multipole method for solving integral equations of three-dimensional topography and basin problems*, Geophysical Journal International, 140 (2000), pp. 198–210.
- [17] D. L. GAZZONI FILHO, G. BRANDÃO, G. ADJ, A. ALBLOOSHI, I. A. CANALES-MARTÍNEZ, J. CHÁVEZ-SAAB, AND J. LÓPEZ, *Pqc-amx: Accelerating saber and frodokem on the apple m1 and m3 socs*, Cryptology ePrint Archive, (2024).
- [18] L. GREENGARD AND V. ROKHLIN, *A fast algorithm for particle simulations*, Journal of computational physics, 73 (1987), pp. 325–348.
- [19] N. HALKO, P.-G. MARTINSSON, AND J. A. TROPP, *Finding structure with randomness: Probabilistic algorithms for constructing approximate matrix decompositions*, SIAM review, 53 (2011), pp. 217–288.
- [20] INTEL CORPORATION, *Intel 64 and IA-32 Architectures Optimization Reference Manual, Volume 1*, 2023, <https://www.intel.com/content/www/us/en/content-details/671488/intel-64-and-ia-32-architectures-optimization-reference-manual-volume-1.html>. Version 049, Last updated: September 5, 2023.
- [21] J. Y. LI, S. AMBIKASARAN, E. F. DARVE, AND P. K. KITANIDIS, *A kalman filter powered by matrices for quasi-continuous data assimilation problems*, Water Resources Research, 50 (2014), pp. 3734–3749.
- [22] D. MALHOTRA, *Fast Integral Equation Solver for Variable Coefficient Elliptic PDEs in Complex Geometries*, doctoral dissertation, The University of Texas at Austin, 2017. Available at.

- <http://hdl.handle.net/2152/63349>.
- [23] D. MALHOTRA AND G. BIROS, *Pvfm: A parallel kernel independent fmm for particle and volume potentials*, Communications in Computational Physics, 18 (2015), pp. 808–830.
 - [24] M. MESSNER, B. BRAMAS, O. COULAUD, AND E. DARVE, *Optimized m2l kernels for the chebyshev interpolation based fast multipole method*, arXiv preprint arXiv:1210.7292, (2012).
 - [25] D. MILES, *Compute intensity and the fft*, in Proceedings of the 1993 ACM/IEEE conference on Supercomputing, 1993, pp. 676–684.
 - [26] NVIDIA CORPORATION, *cuBLAS Library Documentation*, 2024, <https://docs.nvidia.com/cuda/cublas/index.html>. Accessed: 2024-01-29.
 - [27] A. RAHIMIAN, I. LASHUK, S. VEERAPANENI, A. CHANDRAMOWLISHWARAN, D. MALHOTRA, L. MOON, R. SAMPATH, A. SHRINGARPURE, J. VETTER, R. VUDUC, ET AL., *Petascale direct numerical simulation of blood flow on 200k cores and heterogeneous architectures*, (2010), pp. 1–11.
 - [28] T. TAKAHASHI, C. CECKA, W. FONG, AND E. DARVE, *Optimizing the multipole-to-local operator in the fast multipole method for graphical processing units*, International Journal for Numerical Methods in Engineering, 89 (2012), pp. 105–133.
 - [29] F. G. VAN ZEE AND R. A. VAN DE GELIJN, *Blis: A framework for rapidly instantiating blas functionality*, ACM Transactions on Mathematical Software (TOMS), 41 (2015), pp. 1–33.
 - [30] P. VIRTANEN, R. GOMMERS, T. E. OLIPHANT, M. HABERLAND, T. REDDY, D. COURNAPEAU, E. BUROVSKI, P. PETERSON, W. WECKESSER, J. BRIGHT, ET AL., *Scipy 1.0: fundamental algorithms for scientific computing in python*, Nature methods, 17 (2020), pp. 261–272.
 - [31] T. WANG, R. YOKOTA, AND L. A. BARBA, *Exafmm: a high-performance fast multipole method library with c++ and python interfaces*, Journal of Open Source Software, 6 (2021), p. 3145.
 - [32] S. WILLIAMS, A. WATERMAN, AND D. PATTERSON, *Roofline: an insightful visual performance model for multicore architectures*, Communications of the ACM, 52 (2009), pp. 65–76.
 - [33] L. YING, G. BIROS, AND D. ZORIN, *A kernel-independent adaptive fast multipole algorithm in two and three dimensions*, Journal of Computational Physics, 196 (2004), pp. 591–626.